




# COMMUNICATIONS CHEMISTRY

## ARTICLE

<https://doi.org/10.1038/s42004-019-0175-7>

OPEN

## Local accumulation of diacylglycerol alters membrane properties nonlinearly due to its transbilayer activity

Pablo Campomanes<sup>1</sup>, Valeria Zoni<sup>1</sup> & Stefano Vanni <sup>1</sup>

Diacylglycerols (DAGs) are bioactive lipids that are ubiquitously present at low concentrations in cellular membranes. Upon the activation of lipid remodeling enzymes such as phospholipase C and phosphatidic acid phosphatase, DAG concentration increases, leading to a disruption of the lamellar phase of lipid membranes. To investigate the structural origin of these phenomena, here we develop a coarse-grained model for DAGs that is able to correctly reproduce its physicochemical properties, including interfacial tension and flip-flop rate. We find that even at low concentrations a nonnegligible percentage of DAG molecules occupies the interleaflet space. At high concentrations, DAG molecules undergo a phase-separation process from lamellar lipids, segregating in DAG-only blisters and effectively reducing the DAG surface pool available to peripheral enzymes. Our results allow for a better understanding of the role of DAGs in cellular membranes and provide a new tool for the quantitative estimation of low-abundance lipids on membrane properties.

<sup>1</sup>Department of Biology, University of Fribourg, Chemin du Musée 10, 1700 Fribourg, Switzerland. Correspondence and requests for materials should be addressed to S.V. (email: [stefano.vanni@unifr.ch](mailto:stefano.vanni@unifr.ch))

Diacylglycerols (DAGs) are a minor component of cellular membranes, acting as second messengers in a large number of diverse signaling pathways including lipid metabolism, protein export, or neurotransmission<sup>1</sup>. Because of that, they play a crucial role in cellular homeostasis, and misregulation of their concentration might lead to severe conditions such as Alzheimer's disease or cancer<sup>2,3</sup>. Upon specific signaling events, such as calcium-induced phospholipase C (PLC) activation or excessive food intake, the level of DAGs in specific intracellular compartments can increase significantly<sup>4</sup>. At those concentrations, DAGs not only behave as signaling molecules but also significantly alter the physicochemical properties of the membrane, promoting, for example, membrane fusion and fission<sup>5,6</sup>.

While the properties of DAG-enriched membranes have been characterized extensively using experimental methods<sup>7,8</sup>, the structural origin of their behavior has not been convincingly addressed. This stems from the physicochemical nature of DAGs as weak nonionic surfactants, and from intrinsic limitations of molecular dynamics (MD) simulations, the method of choice to simulate lipid assemblies at the structural and dynamical level, when dealing with this type of molecules and, more generally, with phenomena that depend on the accurate reproduction of interfacial tension at liquid/liquid and liquid/air interfaces. These limitations hold true both for all-atom (AA) simulations, which tend to overestimate the transbilayer flip-flop barrier for DAGs<sup>9,10</sup>, and for commonly used coarse-grained (CG) models, which suffer from intrinsic drawbacks when trying to reproduce interfacial tension of liquid/liquid interfaces and pressure-area isotherms<sup>11–13</sup>.

A powerful alternative in this context is the CG force field originally developed by Shinoda, DeVane, and Klein (SDK), which has been shown to reliably reproduce properties at the interface between water and lipids<sup>14–16</sup>. This model appears well adapted to unambiguously characterize the relationship between the molecular features of surfactant-like compounds and their macroscopic physicochemical behavior, including their involvement in large-scale biological events<sup>17</sup>. A major drawback of the SDK model is the relatively low number of distinct beads that are currently available in this force field. This limits the number of different species that can be currently simulated and, therefore, its range of applicability.

To overcome this limitation, we here extend the SDK model by incorporating a new bead (hydroxyl, OG) to treat at the CG level molecules having this functional group, which is commonly found in many compounds that behave as weak surfactants, including DAGs such as dioleoylglycerol (DOG). We show that our model is able to accurately reproduce experimental properties of DAGs such as its interfacial tension with water and its flip-flop free energy barrier in a solvated lipid bilayer, and that it allows capturing morphological changes in the lipid organization of phospholipid membranes induced by variation in DAG concentration.

## Results

**Derivation of a coarse-grained model for diacylglycerols.** The requirement of a new bead (OG) to treat molecules such as DOG (Fig. 1a) at the CG level called for the development of a set of parameters fully compatible with the existent SDK force field. To this end, as a first step, it was needed to identify a series of compounds for which experimental density and/or surface tension data were available in order to determine all the nonbonded Lennard-Jones (LJ) parameters involving OG. The literature values of the selected compounds are collected in Table 1<sup>18–22</sup>. Their mapping can be found in Supplementary Fig. 1.

To improve transferability across chemically related CG molecules and reduce the risk of overfitting, a redundant group of compounds was chosen for the parameterization; i.e., the set selected was composed by molecules that allow to simultaneously refine the original  $\sigma$  and  $\epsilon$  parameters in more than one system, making them concertedly consistent. In particular, the protocol to adjust all new  $\sigma$  and  $\epsilon$  nondiagonal parameters required running hundreds of simulations around educated initial guesses (obtained from the Lorentz–Berthelot combination rules) until  $\sigma$  and  $\epsilon$  values able to jointly reproduce (within the calculated standard deviations) the target density and surface tension data were identified. As illustrated in Fig. 1b and collected in Table 1, which reports the calculated mean values together with the corresponding standard deviations, experimental densities, and surface tensions are very accurately reproduced: mean relative errors for  $\rho$  and  $\gamma$  are lower than 0.9% and 1.9%, respectively. The final set of consistent LJ nonbonded parameters is given in Supplementary Table 1. Interestingly, following the protocol mentioned above, a larger  $\epsilon$  value was found (Supplementary Table 1) for the OG–CMD2 interaction in comparison with those obtained for OG–CT, OG–CT2, OG–CM, and OG–GL. This fact consistently reflects the distinct chemical nature of the OG–CMD2 interaction: while all mentioned hydrocarbon beads (CMD2, CT, CT2, CM, and GL) are basically nonpolar and with a similar effective size (as described by the  $\sigma$  parameter), CMD2 is unique because it presents a nonconjugated C=C double bond in its molecular structure. It is well known that the electronic cloud of this type of  $\pi$ -systems is susceptible to form peculiar hydrogen bonding interactions with hydroxyl groups (here represented by OG beads), and the parameterization protocol employed here seems to accurately reflect this fact by leading to a larger  $\epsilon$ (OG–CMD2) value.

Together with the derivation of the aforementioned LJ parameters, we had to develop parameters for all the bonded interactions that include OG. These parameters, which are given in Supplementary Tables 2 and 3, were set following an iterative procedure until a consistent fit between the bond and angular probability distributions coming from both AA and CG simulations was obtained.

Next, we targeted the interfacial tension values of two alcohols, 1-pentanol and 1-hexanol<sup>23</sup>, to set the nonbonded parameters describing the interaction of OG with water. The pair  $\sigma = 3.6580$  Å and  $\epsilon = 0.7479$  kcal mol<sup>-1</sup> provided the best agreement between experimental and calculated values (Table 2).

Finally, we derived some missing parameters to account for the interaction between DAG and lamellar phospholipids such as phosphatidylcholine (PC). The off-diagonal LJ parameters corresponding to the interaction between the OG and the CG particles that form the PC moiety of DOPC (PH and NC) were determined by using structural information coming from atomistic simulations, and specifically the short-range behavior of the OG–NC and OG–PH radial distribution functions (RDFs). In particular, we used an iterative protocol that was extended until a consistent match in the location of the first peak of the RDFs obtained from the AA and CG simulations was found. Because of the existence of many other interaction terms in the system, which we have not tried to optimize but kept fixed, a perfect match of all the peaks of the RDFs cannot be achieved using a simple LJ potential energy function and more structured RDFs were inevitably obtained from the atomistic simulations (Supplementary Figs. 2 and 3).

**Model validation.** We then evaluated the ability of the parameters composing our new CG model to reproduce known experimental properties of DAGs. First, we estimated the interfacial tension at the DOG/water interface. A very accurate match between experiment<sup>24</sup> (17.2 mN m<sup>-1</sup>) and simulation (17.2 ± 0.8

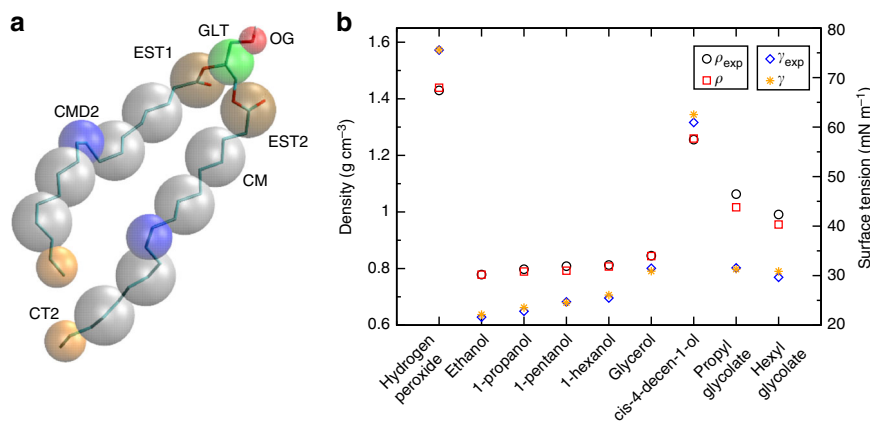


**Fig. 1** CG model derivation for DAGs. **a** All-atom (licorice) to coarse-grained (vdw) mapping for DOG. For better clarity, the hydrogen atoms in the atomistic representation are not displayed. The nomenclature of the different beads was kept consistent with that of previous studies in phospholipids and triglycerides<sup>16,40</sup>. A new particle to account for the hydroxyl group (OG, red) was introduced. **b** Calculated vs experimental density and surface tension values for all the molecules in the data set used to derive the CG model for DAGs

**Table 1** Compounds used in the derivation of the CG model for DAGs. Experimental and calculated density ( $\rho_{\text{exp}}$  and  $\rho_{\text{calc}}$ ) and surface tension ( $\gamma_{\text{exp}}$  and  $\gamma_{\text{calc}}$ ) values are given in  $\text{g cm}^{-3}$  and  $\text{mN m}^{-1}$ , respectively

Compounds	LJ interactions	$\rho_{\text{exp}}$	$\gamma_{\text{exp}}$	$\rho_{\text{calc}}$	$\gamma_{\text{calc}}$	T (K)
H <sub>2</sub> O <sub>2</sub>	OG-OG	1.453	75.94	1.44 ± 0.02	75.6 ± 0.7	291.15
Ethanol	OG-CT2	0.782	21.55	0.778 ± 0.004	22.1 ± 0.3	303.15
1-Propanol	OG-CT	0.797	22.93	0.790 ± 0.009	23.5 ± 0.3	303.15
1-Pentanol	OG-CM	0.808	24.92	0.79 ± 0.01	24.5 ± 0.2	303.15
1-Hexanol	OG-CT2					
	OG-CM	0.816	25.81	0.807 ± 0.006	26.1 ± 0.4	298.15
	OG-CT					
cis-4-decen-ol	OG-CMD2	0.846	31.48	0.844 ± 0.005	30.9 ± 0.4	303.15
	OG-CM					
	OG-CT2					
Glycerol	OG-GLT	1.259	63.40	1.260 ± 0.008	62.5 ± 0.2	293.15
Propylglycolate	OG-EST		31.55		31.3 ± 0.1	293.15
	OG-CT					
Hexylglycolate	OG-EST		29.66		30.9 ± 0.4	293.15
	OG-CM					
	OG-CT					

**Table 2** Experimental and calculated interfacial tensions for the compounds targeted to derive the interaction of OG with water. In both cases, the experimentally measured and computed values were determined at room temperature (298.15 K) and pressure (1 atm)

Compounds	LJ interaction	$\gamma_{\text{exp}}$ ( $\text{mN m}^{-1}$ )	$\gamma_{\text{calc}}$ ( $\text{mN m}^{-1}$ )
1-pentanol	OG-W	4.4	3.3 ± 0.6
1-hexanol	OG-W	6.8	7.3 ± 0.6

$\text{mN m}^{-1}$ ) was found for this system. Next, we prepared a system composed of 46:25:29 in wt% of DOPC/DOG/H<sub>2</sub>O. As previously discussed in the literature<sup>8,25</sup>, under these conditions the system should adopt a stable inverse hexagonal phase. To investigate the stability of this phase, we run a 2- $\mu\text{s}$ -long CG simulation using the force field here developed for DOG. As can be seen in Supplementary Movie 1, all the features of the original phase were maintained during the time scale of our simulations, which further validates our CG model.

To further assess the quality of our model for DAGs, we also estimated the energy barrier associated to the transbilayer

movement of a specific DAG for which the experimental determination of this property is available, dilaureoyl-*sn*-glycerol (DLG), in a palmitoyl oleyl phosphatidylcholine (POPC) bilayer. To do so, we computed the potential of mean force (PMF) associated to the DLG flip-flop movement by using umbrella sampling (US), in the spirit of previous studies on this topic<sup>9,26</sup>, in order to drive the system into high-energy regions and, therefore, evaluate the propensity of DLG to move between leaflets. The projection along the *z*-axis of the distance between the OG bead and the center of the bilayer was chosen as reaction coordinate. The corresponding PMF, as the average of two independent US simulations, is displayed in Fig. 2. The free energy profile reconstructed from these nonequilibrium simulations shows a minimum at about 14.9 Å which correspond to the middle of the bilayer. Moreover, it shows that the barrier that DLG has to overcome to shift from one of the leaflets to the other is of only  $1.4 \pm 0.2 \text{ kcal mol}^{-1}$  (to be compared with the experimentally reported value<sup>10</sup> of about  $2 \text{ kcal mol}^{-1}$ ). This result further corroborates the quality of the model here developed for DAGs by accurately reproducing the experimentally measured free energy barrier for this event. In comparison, AA simulations have reported<sup>9,26</sup> barriers for the flip-flop rate of DAGs in the range of 6–9  $\text{kcal mol}^{-1}$ .

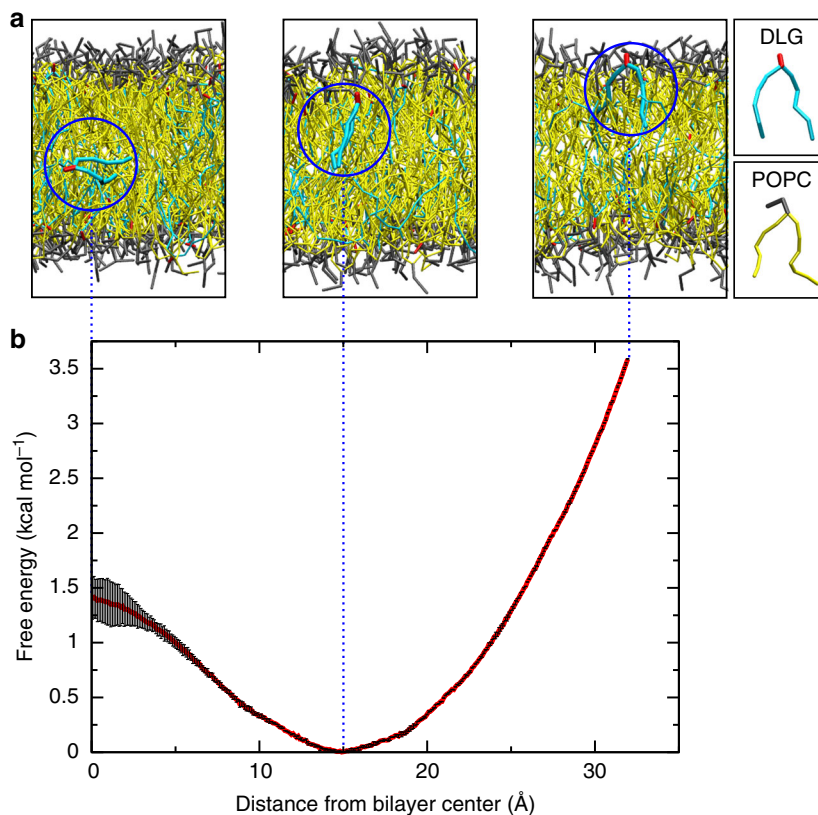


**Fig. 2** Calculation of the potential of mean force associated to DLG flip-flop. **a** Representative snapshots illustrating the movement of the selected DLG molecule along the reaction coordinate. **b** PMF for the transfer of a DLG molecule from bulk water to the center of the POPC bilayer. The harmonic restraint used to calculate the profile was placed on the OG bead of DLG. Two independent US simulations were performed. The average PMF (red) together with the corresponding error bars (black), obtained as the difference between both US simulations, are displayed

### Morphological effects of diacylglycerols on lipid bilayers.

Finally, we studied the behavior of mixed DOPC/DOG bilayers for increasing concentrations of DOG (from 5 to 50 mol%). These systems mimic the effect of PLC on DOPC vesicles, where, over time, DOPC is converted into DOG by the protein enzymatic activity<sup>27</sup>. For what pertains the spatial distribution of DOG molecules in the bilayer, our simulations show that there is a non-negligible probability of finding the hydroxyl group of DOG in the region between both leaflets (near the center of the bilayer) already at low (5%) DOG concentration (Figs. 3 and 4a). In this condition, 8% of the total DOG is entirely immersed in the bilayer, without interacting with either water or the phosphate groups of the DOPC lipids. When increasing the DOG concentration up to a value of 20%, the fraction of DOG that is entirely immersed in the bilayer remains constant (Fig. 4b). Above this value, the DOG population inside the bilayer increases significantly, while the amount of DOG at the bilayer/water interface, and hence available to interact with peripheral enzymes, plateaus to a concentration of 25% regardless of the total amount of DOG initially present in the bilayer, in agreement with experiments suggesting that the miscibility limit of DOG in unsaturated PC lipids is of 0.25 molar fraction<sup>28,29</sup>. Of note, this behavior is accompanied by a sharp change in the flip-flop barrier, as computed by Boltzmann inverting the populations obtained in the lateral density profiles (Supplementary Table 4), that also drastically decreases for DOG concentrations above 20%.

Notably, above a DOPC:DOG molar ratio of 60:40, the system undergoes a spontaneous phase-separation process, with a large portion of DOG molecules accumulating between the two leaflets

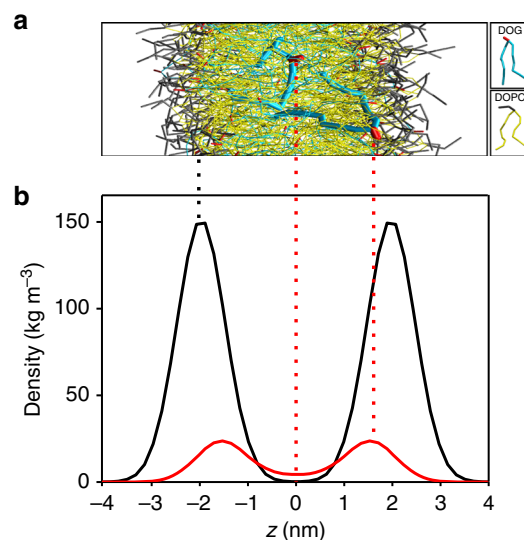


**Fig. 3** Spatial distribution of DOG in the bilayer. **a** Snapshots of two representative DOG molecules. **b** Mass density profiles for the hydroxyl group (OG bead) in DOG (red) and the phosphate group (PH bead) in POPC (black)

of the bilayer and forming a lens with a thickness of  $10.2 \pm 0.3$  nm at its maximum (Fig. 4c). This suggests that, above a certain DOG concentration, the membrane saturates and the excess of DOG must be stored in the interior of the bilayer. Interestingly, this

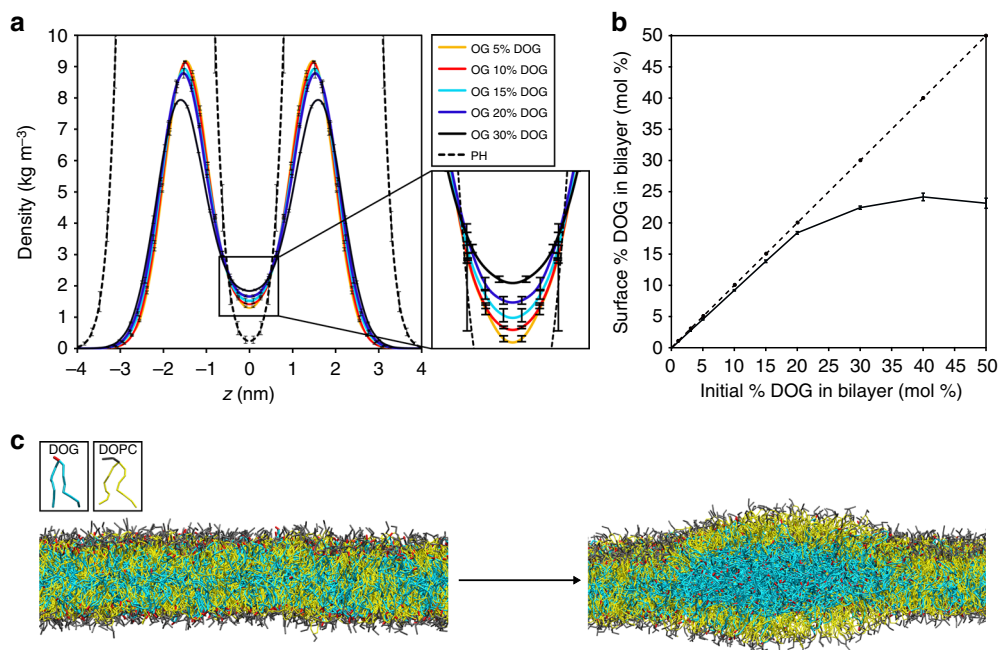


**Fig. 4** Lipid organization changes at increasing DAGs concentration. **a** Normalized density profile for the OG bead in DOG at different DOG:DOPC mole ratio. Error bars are obtained as standard deviation from two independent simulations. **b** Initial and final concentration of DOG (mol%) at the water/bilayer interface (solid line). The dashed line represents the theoretical concentration of DOG if no DOG molecules were immersed in the bilayer. Error bars indicate standard deviation over the last 1  $\mu$ s of the MD trajectory. **c** DOG lens formation in a bilayer with DOPC (yellow) and DOG (blue) in a molar ratio of 60:40. DOPC headgroups are colored in gray, while OG beads are highlighted in red

DOG concentration-induced change in the lipid organization of the DOPC/DOG mixture is consistent with the findings of recent spectroscopic experiments that reported a transition from a lamellar composition to a biphasic mixture when the percentage of DAG in a POPC bilayer was increased from 10 to 50%<sup>30</sup>, as well as with previous studies on the activity of PLC on giant unilamellar vesicles<sup>31,32</sup>. This rearrangement at high DOG concentration reveals the dual nature of DAGs that, because of the presence of a small polar headgroup in their structure, show an intermediate behavior between that of oils and that of phospholipids.

## Discussion

In membranes, DAGs are generally believed to adopt a conformation that is similar to that of phospholipids, with their hydroxyl group pointing towards water and their hydrophobic chains residing in the membrane hydrophobic core. Our simulations indicate that this assumption is mostly correct at low DAG concentrations, but becomes less accurate with increasing DAG content. Indeed, at high DAG concentration, we observed a mechanism of lens formation by DAG that is akin to a similar spontaneous process observed in MD simulations of lipid bilayers enriched with triacylglycerol (TAG), of which DAG is a precursor<sup>33</sup>.

This reflects similar physicochemical properties of TAG and DAG, but also highlights important differences between the two. First, TAG has a significantly higher interfacial tension with water ( $32 \text{ mN m}^{-1}$  vs  $17.2 \text{ mN m}^{-1}$ ) and mostly resides in the interior of the bilayer at low concentrations<sup>33,34</sup>. Second, blister formation of TAG happens at a much lower concentration ( $\sim 5\%$ ) than DAG<sup>33</sup>. Third, while TAG blisters do exist in cells, where they have been proposed to represent the early step of lipid droplet (LD) formation in the endoplasmic reticulum<sup>35</sup>, DAG blisters have not been observed, since in the absence of the last step of TAG synthesis, i.e., DAG esterification, fluorescent staining of the

hydrophobic core of intracellular membranes does not show a punctate localization typical of LDs, but rather remains diffuse in the endoplasmic reticulum<sup>36</sup>.

Remarkably, cholesterol has a somewhat similar amphipathic structure to that of DAGs, with a large hydrophobic region and a small polar head consisting of only a hydroxyl group. Cholesterol has also been shown to reside partly in the interior of lipid bilayers consisting of polyunsaturated phospholipids, using a combination of neutron scattering and MD simulations<sup>37</sup>. Unlike DAGs, however, cholesterol is known to be present at high concentration ( $\sim 50\%$ ) in saturated or monounsaturated phospholipid bilayers without disrupting their lamellar phase. We speculate that the molecular origin of this difference could be twofold: on the one hand, cholesterol, unlike DAG, establishes preferential interactions with saturated and unsaturated tails of phospholipids due to its unique rigid-rings molecular structure<sup>38</sup>, on the other hand DAGs, and especially DOG (intrinsic molecular curvature  $\zeta_{\text{DOG}} = -1 \text{ nm}^{-1}$ ) have a markedly higher inverted conical shape than cholesterol ( $\zeta_{\text{CHOL}} = -0.4 \text{ nm}^{-1}$ )<sup>8,39</sup>.

In fact, because of their shape DAGs are known to form nonlamellar hexagonal or cubic phases at low hydration levels<sup>25</sup> and have even been proposed to promote such phases in biological membranes. Our simulations, however, suggest that in the presence of excess water, as is the case in a physiological context, DAGs rather partially sequester in the interior of the lipid membrane.

In summary, we present here a new CG model for DAGs that is fully compatible with the SDK force field and that is able to accurately reproduce experimental properties of DAGs such as its interfacial tension with water and its flip-flop free energy barrier in a solvated lipid bilayer. This model allows to capture morphological changes in the lipid organization of phospholipid membranes induced by variation in DAG concentration. Moreover, thanks to the strategy employed in the parameterization, the same nonbonded parameters developed in this work can be used to treat other species with a hydroxyl group in a similar chemical

environment; therefore, no modifications are required to describe chemically related OH-containing compounds such as lysolipids or fatty alcohols.

## Methods

**Coarse-grained force field derivation.** The protocol to derive CG parameters compatible with the SDK force field involved several steps. First, in order to develop a CG model for DAGs, an AA to CG mapping, consistent with those previously described for phospholipids and triglycerides<sup>16,40</sup>, was defined. To this end, only a new bead for the hydroxyl group (OG) had to be introduced. Then, we selected a series of representative OH-containing molecules constructed from the beads defined in the previous step and run one-component atomistic simulations for each of the compounds in this set. This allowed us, using the procedure detailed elsewhere<sup>14,41</sup>, to determine all the bonded and nonbonded LJ parameters involving the new bead. In short, the CG bonded parameters (equilibrium values and force constants for bonds and angles) were adjusted to reproduce the averages and standard deviations of the bond and angular probability distributions of the corresponding mapped atomistic simulations, whereas the CG nonbonded parameters were determined by targeting experimental density and surface tension data. Finally, as the quality of the model was assessed by examining its ability to estimate the surface tension of DOG at the interface with water and the flip-flop rate of DLG in a solvated POPC bilayer, and to mimic the experimentally known behavior of mixed DOPC/DOG bilayers for increasing concentrations of DOG, the off-diagonal LJ parameters corresponding to the interaction of OG with both water and the PC headgroups had to be estimated. In the case of water, they were derived by using interfacial tension as the target property. On the other hand, the parameters for the interaction with the PC headgroups were determined by using structural information coming from atomistic simulations, RDFs in particular, as targets. The methodologies used in these steps are discussed in more detail below.

**Coarse-grained mapping.** To keep consistency with the mapping previously developed for phospholipids<sup>16</sup>, in which individual CG particles were used to represent the glycerol moiety and each of the ester groups forming these compounds, only a new bead (OG), to account for the hydroxyl group, was introduced in order to develop the CG model for DAGs. The definition of the CG sites for the hydrophobic lipid tails was also carried out adopting a strategy analogous to that employed in previous studies; accordingly, each bead consistently contains two or three carbon atoms and the hydrogens bound to them. All beads were placed in the center of mass of all the atoms defining it.

**Coarse-grained model.** The CG model utilized here uses simple potential energy functions to describe the interaction between beads. In particular, bonded terms are represented by means of harmonic potentials ( $U_{\text{bond}}$  and  $U_{\text{angle}}$ ) and, to prevent angle collapses when small angle force constants are employed, an ad hoc 1–3 repulsive term between tuples of beads connected by two consecutive bonds ( $U^{\text{corr}}$ ) is incorporated in the angle potential expression. On the other hand, the non-bonded interactions between neutral beads are described using LJ potentials. A 12–4 functional form is employed to model interactions where water is involved, while a 9–6 LJ expression is used for interactions between other beads.

$$U_{\text{bond}} = \sum_{\text{bonds}} k_b (r_{ij} - r_0)^2 \quad (1)$$

$$U_{\text{angle}} = \sum_{\text{angles}} k_\theta (\theta_{ijk} - \theta_0)^2 + U^{\text{corr}} \quad (2)$$

$$U^{\text{corr}} = \sum_{\text{angles}} [U_{\text{LJ}}(r_{ij}) - U_{\text{LJ}}(\sigma_{ij})] \quad (\text{for } r_{ij} < \sigma_{ij}) \quad (3)$$

$$U_{\text{LJ}}(r_{ij}) = \begin{cases} \frac{3\sqrt{3}}{2} \epsilon_{ij} \left[ \left( \frac{\sigma_{ij}}{r_{ij}} \right)^{12} - \left( \frac{\sigma_{ij}}{r_{ij}} \right)^4 \right] & (\text{for pairs with water}) \\ \frac{27}{4} \epsilon_{ij} \left[ \left( \frac{\sigma_{ij}}{r_{ij}} \right)^9 - \left( \frac{\sigma_{ij}}{r_{ij}} \right)^6 \right] & (\text{for other pairs}) \end{cases} \quad (4)$$

**All-atom molecular dynamics.** Atomistic simulations of various OH-containing molecules were performed to generate the reference data required to parameterize the bonded terms of the CG potential. Typically, suitable starting configurations for these systems (comprising 512 identical molecules) were built using PACKMOL<sup>42</sup>. All simulations were carried out under periodic boundary conditions using the GROMACS package<sup>43,44</sup>. The force field parameters to describe hydrogen peroxide and glycerol were adopted from previous studies<sup>45,46</sup> whereas parameters compatible with the CHARMM 36 force field<sup>47,48</sup>, generated via the CHARMM-GUI interface<sup>49,50</sup>, were employed for the other molecules used in the derivation of the new DAG force field. The long-range electrostatic interactions were taken into account using the particle mesh Ewald algorithm<sup>51</sup> with a Fourier grid spacing of 1.5 Å and a real space cutoff of 12 Å. The van der Waals interactions were truncated using the same cutoff, and a standard smoothing function for the tail region

(10–12 Å) was employed. The bonds involving hydrogen atoms were constrained using the LINCS algorithm<sup>52</sup>, thus allowing the usage of an integration time step of 2 fs. All simulations were performed in the NPT ensemble. The temperature and pressure were controlled by coupling the system to a stochastic velocity rescaling thermostat<sup>53</sup> and a Parrinello–Rahman barostat<sup>54</sup>, respectively. After a short equilibration period, all simulations were run for 40 ns to lead to well-converged bond and angular distributions.

**Coarse-grained molecular dynamics.** Representative snapshots of each of the aforementioned one-component atomistic MD simulations were mapped into CG representations with the help of the CG-it software (<https://github.com/CG-it>) and employed as initial configurations for the CG–MD runs. An integration time step of 10 fs was employed in all simulations, which were carried out with LAMMPS (<http://lammps.sandia.gov>)<sup>55,56</sup>. Nonbonded interactions were truncated using a 15 Å cutoff. All CG parameters not comprising the new OG bead were adopted from previous studies<sup>14,16,40</sup>. The runs executed to fix the bonded parameters involving OG were conducted in the NPT ensemble using a Nosé–Hoover thermostat<sup>57</sup> and barostat<sup>54,58,59</sup> to control the temperature and pressure, respectively. The determination of these parameters was performed iteratively by means of sequential 5 ns runs, long enough to relax the molecular structures of the species involved, until a good fit was obtained. The CG nonbonded parameters describing the interaction of OG with the other beads in the DOG molecule were adjusted by running hundreds of simulations in a range of  $\sigma$  and  $\epsilon$  values covering a sufficiently wide area around initial guesses that were obtained using the Lorentz–Berthelot combination rules<sup>60,61</sup>. The LJ parameters able to jointly reproduce, with the best accuracy, the target experimental density and surface tension were selected. The simulations performed to compute the average density were evolved in the NPT ensemble and extended for 5 ns, whereas those carried out to calculate the corresponding surface tension were performed in the NVT ensemble after increasing the cell length along one of the axis ( $z$ -axis) by 40 nm to create the required vacuum/liquid interfaces. In the latter case, 30 ns was typically needed to get converged values. The surface tension was computed from the diagonal values of the pressure tensor ( $P_{xx}$ ,  $P_{yy}$ , and  $P_{zz}$ ), using the Kirkwood–Irving method<sup>62</sup>, as follows:

$$\gamma = \frac{L}{2} \left( \langle P_{zz} \rangle - \frac{P_{xx} + P_{yy}}{2} \right) \quad (5)$$

where  $L$  represents the box length along  $z$  and  $\langle \dots \rangle$  denotes ensemble average.

**Coarse-grained force field validation.** As previously mentioned, the quality of the CG model developed was assessed by verifying its ability to accurately predict experimental properties of DAGs. In particular, we aimed at reproducing the surface tension of DOG at the interface with water, the flip-flop rate of DLG in a solvated POPC bilayer and the behavior of mixed DOPC/DOG bilayers for increasing concentrations of DOG. To this end, it was required to initially determine the LJ parameters corresponding to the interaction between OG and water, and then derive those characterizing the interaction between the OG and the PC group.

**DOG interfacial tension.** The nonbonded parameters to describe the interaction of OG with water were fixed by targeting the interfacial tensions experimentally measured for the mixtures between alcohols (1-pentanol and 1-hexanol in particular) and water<sup>23</sup>. The protocol used was similar to that previously described when looking at density and surface tension data; i.e., a series of short simulations (30 ns) with distinct OG–W  $\sigma$  and  $\epsilon$  values (chosen to sample a relatively broad area around initial estimates derived from the Lorentz–Berthelot standard combination rules) were carried out, and the values jointly leading to the best fit were selected. Initial configurations for these simulations were generated from equilibrated snapshots of the trajectories used to calculate the average densities. To create the required interface with water, the corresponding cells were elongated along the  $z$ -axis by 60 Å and filled with water molecules before starting the dynamics. The runs were performed with the lateral  $x$  and  $y$  dimensions constrained to their original values while the orthogonal  $z$  dimension was allowed to fluctuate. As previously, the temperature and pressure were controlled by means of a Nosé–Hoover thermostat<sup>57</sup> and barostat<sup>54,58,59</sup>, respectively. The starting configuration of the simulation carried out to calculate the DOG interfacial tension was built in an analogous way. In this case, the final snapshot of an 80 ns run conducted to equilibrate an orthogonal and periodic simulation box containing 512 DAG molecules (originally placed in random positions) was selected as equilibrated snapshot. This configuration was then elongated along the  $z$ -axis, and the empty space was filled with water molecules.

**DLG flip-flop rate in POPC bilayer.** To determine the parameters for the interactions between OG and the CG particles (PH and NC) composing the PC moiety of the phospholipids, we computed the OG–PH and OG–NC RDFs from atomistic simulations carried out on a DOPC/DOG mixed bilayer at an 85:15 molar ratio and then maximized their match with those calculated using CG–MD. The reference trajectory was taken from a previous study<sup>26</sup>. A representative frame was extracted from this trajectory and mapped into the corresponding CG representation before starting the iterative search of the OG–PH and OG–NC nonbonded parameters

that better reproduce the short-range features of the atomistic RDFs. The runs were evolved in the NPT ensemble for 40 ns using semi-isotropic coupling to control cell fluctuations. Nonbonded interactions were truncated using a 15 Å cutoff, and an integration time step of 10 fs was employed in all simulations. Moreover, a particle–particle particle–mesh (PPPM) solver<sup>63,64</sup> with an RMS force error of 10<sup>-5</sup> kcal mol<sup>-1</sup> Å<sup>-1</sup> and an order of three was employed to compute the long-range electrostatic interactions beyond the aforementioned cutoff. Upon determination of the OG–PH and OG–NC LJ parameters, DOG and DOPC were mutated into DLG and POPC, respectively, in order to build a DLG/POPC system. This mixed bilayer was then replicated (3 × 3) in the lateral directions (x and y) to avoid undesirable size effects in the calculation of the free energy profile associated to the DLG flip-flop movement. The z-component of the distance between the OG bead of a randomly chosen DLG molecule and the membrane center (defined as the center of mass of all the POPC glycerol beads) was chosen as reaction coordinate,  $\xi$ . US<sup>65</sup>, using the collective variables module for LAMMPS<sup>66</sup>, was employed to overcome poor sampling at energetically unfavorable configurations and estimate the PMF along  $\xi$ . A simple harmonic function was employed for the distance restraint potential.

$$V(\xi) = \frac{1}{2}k(\xi - \xi_0)^2 \quad (6)$$

To allow for an adequate overlap between adjacent windows, altogether covering the region  $0 < |\xi| < 32$  Å, umbrella simulations were started from 17 equispaced  $\xi_0$  values (with a 2 Å spacing between them). A force constant,  $k$ , of 1.0 kcal mol<sup>-1</sup> Å<sup>-2</sup> was applied to restrain  $\xi$  from sampling values very distant from the minimum of the bias potential ( $\xi_0$ ). A production run of 200 ns was carried out for every window. The initial configurations for each window were generated by pulling the selected DLG molecule with a force of 1.2 kcal mol<sup>-1</sup> Å<sup>-2</sup> towards either the center of the membrane or the bulk solvent until fully covering the range of  $\xi$  values under study ( $0 < |\xi| < 32$  Å). The umbrella histograms representing the biased probability distributions obtained for each of the windows were combined to reconstruct the free energy profile along  $\xi$  using the weighted histogram analysis method<sup>67</sup>. Two independent US simulations, differing on the initial location (upper or lower leaflet) of the DLG molecule whose movement was biased, were performed. As a consequence, we obtained a PMF per leaflet, and the final PMF together with the associated error were estimated as the mean and standard deviation, respectively, over the two leaflets.

**DOPC/DOG bilayers at different DOG concentrations.** Initial configurations and input files for the different DOPC/DOG bilayers were obtained through conversion of atomistic snapshots using the aforementioned CG-it software. The atomistic configurations were built using the CHARMM–GUI interface. The CG bilayers were composed of 3200 lipids, with different DOPC:DOG ratios (from 95:5 to 50:50). To investigate the spatial distribution of the different molecules during the dynamics, 1.5- $\mu$ s-long CG equilibrium simulations were performed on these mixed bilayers, and lateral density profiles were calculated from these runs using GROMACS tools. DOG flip-flop barriers for the various DOPC:DOG compositions were estimated by Boltzmann inverting the populations obtained in the above-mentioned lateral density profiles according to

$$A(\xi) = -kT \ln P(\xi) \quad (7)$$

## Data availability

The authors declare that all data supporting the findings of this study are available within the paper or can be obtained from them upon request.

Received: 15 December 2018 Accepted: 7 June 2019

Published online: 25 June 2019

## References

- Goñi, F. M. & Alonso, A. Structure and functional properties of diacylglycerols in membranes. *Prog. Lipid Res.* **38**, 1–48 (1999).
- Koss, H., Bunney, T. D., Behjati, S. & Katan, M. Dysfunction of phospholipase C $\gamma$  in immune disorders and cancer. *Trends Biochem. Sci.* **39**, 603–611 (2014).
- Yang, Y. R. et al. Primary phospholipase C and brain disorders. *Adv. Biol. Regul.* **61**, 80–85 (2016).
- Carrasco, S. & Mérida, I. Diacylglycerol, when simplicity becomes complex. *Trends Biochem. Sci.* **32**, 27–36 (2007).
- Gómez-Fernández, J. C. & Corbalán-García, S. Diacylglycerols, multivalent membrane modulators. *Chem. Phys. Lipids* **148**, 1–25 (2007).
- Furt, F. & Moreau, P. Importance of lipid metabolism for intracellular and mitochondrial membrane fusion/fission processes. *Int. J. Biochem. Cell Biol.* **41**, 1828–1836 (2009).
- Leikin, S., Kozlov, M. M., Fuller, N. L. & Rand, R. P. Measured effects of diacylglycerol on structural and elastic properties of phospholipid membranes. *Biophys. J.* **71**, 2623–2632 (1996).
- Szule, J. A., Fuller, N. L. & Rand, R. P. The effects of acyl chain length and saturation of diacylglycerols and phosphatidylcholines on membrane monolayer curvature. *Biophys. J.* **83**, 977–984 (2002).
- Bennett, W. F. D. & Tieleman, D. P. Molecular simulation of rapid translocation of cholesterol, diacylglycerol, and ceramide in model raft and nonraft membranes. *J. Lipid Res.* **53**, 421–429 (2012).
- Hamilton, J. A., Bhamidipati, S. P., Kodali, D. R. & Small, D. M. The interfacial conformation and transbilayer movement of diacylglycerols in phospholipid bilayers. *J. Biol. Chem.* **266**, 1177–1186 (1991).
- Baoukina, S., Marrink, S. J. & Tieleman, D. P. Lateral pressure profiles in lipid monolayers. *Faraday Discuss.* **144**, 393–409 (2010).
- Ollila, O. H. S., Lamberg, A., Lehtivaara, M., Koivuniemi, A. & Vattulainen, I. Interfacial tension and surface pressure of high density lipoprotein, low density lipoprotein, and related lipid droplets. *Biophys. J.* **103**, 1236–1244 (2012).
- Baoukina, S., Monticelli, L., Marrink, S. J. & Tieleman, D. P. Pressure-area isotherm of a lipid monolayer from molecular dynamics simulations. *Langmuir* **23**, 12617–12623 (2007).
- Shinoda, W., DeVane, R. & Klein, M. L. Multi-property fitting and parameterization of a coarse grained model for aqueous surfactants. *Mol. Simul.* **33**, 27–36 (2007).
- Shinoda, W., DeVane, R. & Klein, M. L. Coarse-grained molecular modeling of non-ionic surfactant self-assembly. *Soft Matter* **4**, 2454–2462 (2008).
- Shinoda, W., DeVane, R. & Klein, M. L. Zwitterionic lipid assemblies: molecular dynamics studies of monolayers, bilayers, and vesicles using a new coarse grain force field. *J. Phys. Chem. B* **114**, 6836–6849 (2010).
- Shinoda, W., DeVane, R., Klein, M. L., Fernandez-Recio, J. & Verma, C. Computer simulation studies of self-assembling macromolecules. *Curr. Opin. Struct. Biol.* **22**, 175–186 (2012).
- Tsykalo, A. L. & Tabachnikov, A. G. Density, viscosity, and bond energy of molecules in aqueous hydrogen peroxide solutions. *Theor. Exp. Chem.* **2**, 604–605 (1966).
- Wohlfarth, C., Wohlfarth, B. & Lechner, M. D. *Surface Tension of Pure Liquids and Binary Liquid Mixtures*. (Springer, Berlin, Germany, 2006).
- Jasper, J. J. The surface tension of pure liquid compounds. *J. Phys. Chem. Ref. Data* **1**, 841–1010 (1972).
- Laws, C. L. *Thermophysical Properties of Chemicals and Hydrocarbons*. (Elsevier, Austin, US, 2014).
- Shafrin, E. G. & Zisman, W. A. Effect of progressive fluorination of a fatty acid on the wettability of its adsorbed monolayer. *J. Phys. Chem.* **66**, 740–748 (1962).
- Villers, D. & Platten, J. K. Temperature dependence of the interfacial tension between water and long-chain alcohols. *J. Phys. Chem.* **92**, 4023–4024 (1988).
- Nakajima, Y. Water-retaining ability of diacylglycerol. *J. Am. Oil Chem. Soc.* **81**, 907–912 (2004).
- Orädd, G., Lindblom, G., Fontell, K. & Ljusberg-Wahren, H. Phase diagram of soybean phosphatidylcholine–diacylglycerol–water studied by x-ray diffraction and 31P- and pulsed field gradient 1H-NMR: evidence for reversed micelles in the cubic phase. *Biophys. J.* **68**, 1856–1863 (1995).
- Vamparys, L. et al. Conical lipids in flat bilayers induce packing defects similar to that induced by positive curvature. *Biophys. J.* **104**, 585–593 (2013).
- Cocco, L., Follo, M. Y., Manzoli, L. & Suh, P.-G. Phosphoinositide-specific phospholipase C in health and disease. *J. Lipid Res.* **56**, 1853–1860 (2015).
- Smaby, J. M. & Brockman, H. L. Miscibility, chain packing, and hydration of 1-palmitoyl-2-oleoyl phosphatidylcholine and other lipids in surface phases. *Biophys. J.* **48**, 701–707 (1985).
- Cunningham, B. A., Tsujita, T. & Brockman, H. L. Enzymatic and physical characterization of diacylglycerol–phosphatidylcholine interactions in bilayers and monolayers. *Biochemistry* **28**, 32–40 (1989).
- Holme, M. N. et al. Fate of liposomes in the presence of phospholipase C and D: from atomic to supramolecular lipid arrangement. *ACS Cent. Sci.* **4**, 1023–1030 (2018).
- Riske, K. A. & Döbereiner, H. G. Diacylglycerol-rich domain formation in giant stearoyl-oleoyl phosphatidylcholine vesicles driven by phospholipase C activity. *Biophys. J.* **85**, 2351–2362 (2003).
- Holopainen, J. M., Angelova, M. I., Söderlund, T. & Kinnunen, P. K. J. Macroscopic consequences of the action of phospholipase C on giant unilamellar liposomes. *Biophys. J.* **83**, 932–943 (2002).
- Khandelia, H., Duellund, L., Pakkanen, K. I. & Ipsen, J. H. Triglyceride blisters in lipid bilayers: implications for lipid droplet biogenesis and the mobile lipid signal in cancer cell membranes. *PLoS ONE* **5**, e12811 (2010).
- M'barek, K. Ben, Ajajji, D., Thiam, A. R. & Al, E. ER membrane phospholipids and surface tension control cellular lipid droplet formation. *Dev. Cell* **41**, 591–604.e7 (2017).
- Choudhary, V., Ojha, N., Golden, A. & Prinz, W. A. A conserved family of proteins facilitates nascent lipid droplet budding from the ER. *J. Cell Biol.* **211**, 261–271 (2015).
- Sandager, L. et al. Storage lipid synthesis is non-essential in yeast. *J. Biol. Chem.* **277**, 6478–6482 (2002).

37. Marrink, S. J. et al. Cholesterol shows preference for the interior of polyunsaturated lipid membranes. *J. Am. Chem. Soc.* **130**, 10–11 (2008).
38. Lund-Katz, S., Laboda, H. M., McLean, L. R. & Phillips, M. C. Influence of molecular packing and phospholipid type on rates of cholesterol exchange. *Biochemistry* **27**, 3416–3423 (1988).
39. Chen, Z. & Rand, R. P. The influence of cholesterol on phospholipid membrane curvature and bending elasticity. *Biophys. J.* **73**, 267–276 (1997).
40. Bacle, A., Gautier, R., Jackson, C. L., Fuchs, P. F. J. & Vanni, S. Interdigitation between triglycerides and lipids modulates surface properties of lipid droplets. *Biophys. J.* **112**, 1417–1430 (2017).
41. MacDermaid, C. M. et al. Molecular dynamics simulations of cholesterol-rich membranes using a coarse-grained force field for cyclic alkanes. *J. Chem. Phys.* **143**, 243144 (2015).
42. Martínez, L., Andrade, R., Birgin, E. G. & Martínez, J. M. PACKMOL: a package for building initial configurations for molecular dynamics simulations. *J. Comput. Chem.* **30**, 2157–2164 (2009).
43. Pronk, S. et al. GROMACS 4.5: a high-throughput and highly parallel open source molecular simulation toolkit. *Bioinformatics* **29**, 845–854 (2013).
44. Hess, B., Kutzner, C., Van Der Spoel, D. & Lindahl, E. GROMACS 4: algorithms for highly efficient, load-balanced, and scalable molecular simulation. *J. Chem. Theory Comput.* **4**, 435–447 (2008).
45. Campomanes, P., Rothlisberger, U., Alfonso-Prieto, M. & Rovira, C. The molecular mechanism of the catalase-like activity in horseradish peroxidase. *J. Am. Chem. Soc.* **137**, 11170–11178 (2015).
46. Hatcher, E. R., Guvench, O. & MacKerell, A. D. CHARMM additive all-atom force field for acyclic polyalcohols, acyclic carbohydrates, and inositol. *J. Chem. Theory Comput.* **5**, 1315–1327 (2009).
47. Vanommeslaeghe, K. et al. CHARMM general force field: a force field for drug-like molecules compatible with the CHARMM all-atom additive biological force fields. *J. Comput. Chem.* **31**, 671–690 (2010).
48. Klauda, J. B. et al. Update of the CHARMM all-atom additive force field for lipids: validation on six lipid types. *J. Phys. Chem. B* **114**, 7830–7843 (2010).
49. Jo, S., Kim, T., Iyer, V. G. & Im, W. CHARMM-GUI: a web-based graphical user interface for CHARMM. *J. Comput. Chem.* **29**, 1859–1865 (2008).
50. Lee, J. et al. CHARMM-GUI input generator for NAMD, GROMACS, AMBER, openMM, and CHARMM/openMM simulations using the CHARMM36 additive force field. *J. Chem. Theory Comput.* **12**, 405–413 (2016).
51. Essmann, U. et al. A smooth particle mesh Ewald method. *J. Chem. Phys.* **103**, 8577–8593 (1995).
52. Hess, B. P.-L. I. N. C. S. A parallel linear constraint solver for molecular simulation. *J. Chem. Theory Comput.* **4**, 116–122 (2008).
53. Bussi, G., Donadio, D. & Parrinello, M. Canonical sampling through velocity rescaling. *J. Chem. Phys.* **126**, 014101 (2007).
54. Parrinello, M. & Rahman, A. Polymorphic transitions in single crystals: a new molecular dynamics method. *J. Appl. Phys.* **52**, 7182–7190 (1981).
55. Plimpton, S. Fast parallel algorithms for short-range molecular dynamics. *J. Comput. Phys.* **117**, 1–19 (1995).
56. Brown, W. M., Wang, P., Plimpton, S. J. & Tharrington, A. N. Implementing molecular dynamics on hybrid high performance computers—short range forces. *Comput. Phys. Commun.* **182**, 898–911 (2011).
57. Nosé, S. A molecular dynamics method for simulations in the canonical ensemble. *Mol. Phys.* **52**, 255–268 (1984).
58. Martyna, G. J., Tobias, D. J. & Klein, M. L. Constant pressure molecular dynamics algorithms. *J. Chem. Phys.* **101**, 4177–4189 (1994).
59. Shinoda, W., Shiga, M. & Mikami, M. Rapid estimation of elastic constants by molecular dynamics simulation under constant stress. *Phys. Rev. B* **69**, 134103 (2004).
60. Lorentz, H. A. Ueber die Anwendung des Satzes vom Virial in der kinetischen Theorie der Gase. *Ann. Phys.* **248**, 127–136 (1881).
61. Berthelot, D. Sur le mélange des gaz. *Compt. Rendus* **126**, 1703–1706 (1898).
62. Irving, J. H. & Kirkwood, J. G. The statistical mechanical theory of transport processes. IV. The equations of hydrodynamics. *J. Chem. Phys.* **18**, 817–829 (1950).
63. Eastwood, J. W., Hockney, R. W. & Lawrence, D. N. P3M3DP—the three-dimensional periodic particle-particle/particle-mesh program. *Comput. Phys. Commun.* **35**, C618–C619 (1984).
64. Brown, W. M., Kohlmeyer, A., Plimpton, S. J. & Tharrington, A. N. Implementing molecular dynamics on hybrid high performance computers—particle-particle particle-mesh. *Comput. Phys. Commun.* **183**, 449–459 (2012).
65. Torrie, G. M. & Valleau, J. P. Nonphysical sampling distributions in Monte Carlo free-energy estimation: umbrella sampling. *J. Comput. Phys.* **23**, 187–199 (1977).
66. Fiorin, G., Klein, M. L. & Hémin, J. Using collective variables to drive molecular dynamics simulations. *Mol. Phys.* **111**, 3345–3362 (2013).
67. Kumar, S., Rosenberg, J. M., Bouzida, D., Swendsen, R. H. & Kollman, P. A. The weighted histogram analysis method for free-energy calculations on biomolecules. I. The method. *J. Comput. Chem.* **13**, 1011–1021 (1992).

## Acknowledgements

This work was supported by a grant from the Swiss National Supercomputing Centre (CSCS) under project ID s726 and s842. All authors acknowledge the support of the Swiss National Science Foundation grant #163966.

## Author contributions

P.C. and S.V. designed the project; P.C. and S.V. derived the CG parameters for DAGs; P.C. and V.Z. performed the simulations and analyses to validate the parameterization; P.C., V.Z. and S.V. interpreted the results and wrote the manuscript.

## Additional information

**Supplementary information** accompanies this paper at <https://doi.org/10.1038/s42004-019-0175-7>.

**Competing interests:** The authors declare no competing interests.

**Reprints and permission** information is available online at <http://npg.nature.com/reprintsandpermissions/>

**Publisher's note:** Springer Nature remains neutral with regard to jurisdictional claims in published maps and institutional affiliations.



**Open Access** This article is licensed under a Creative Commons Attribution 4.0 International License, which permits use, sharing, adaptation, distribution and reproduction in any medium or format, as long as you give appropriate credit to the original author(s) and the source, provide a link to the Creative Commons license, and indicate if changes were made. The images or other third party material in this article are included in the article's Creative Commons license, unless indicated otherwise in a credit line to the material. If material is not included in the article's Creative Commons license and your intended use is not permitted by statutory regulation or exceeds the permitted use, you will need to obtain permission directly from the copyright holder. To view a copy of this license, visit <http://creativecommons.org/licenses/by/4.0/>.

© The Author(s) 2019